Nuclear Inst. and Methods in Physics Research, A 1045 (2023) 167532

Contents lists available at ScienceDirect

Nuclear Inst. and Methods in Physics Research, A

journal homepage: www.elsevier.com/locate/nima

First measurements of *remoTES* cryogenic calorimeters: Easy-to-fabricate particle detectors for a wide choice of target materials

G. Angloher [a], M.R. Bharadwaj [a], I. Dafinei [b], N. Di Marco [c,d], L. Einfalt [e,f], F. Ferroni [c,b], S. Fichtinger [e], A. Filipponi [g,d], T. Frank [a], M. Friedl [e], A. Fuss [e,f], Z. Ge [h], M. Heikinheimo [i], K. Huitu [i], M. Kellermann [a], R. Maji [e,f], M. Mancuso [a], L. Pagnanini [c,d], F. Petricca [a], S. Pirro [d], F. Pröbst [a], G. Profeta [g,d], A. Puiu [c,d], F. Reindl [e,f,*], K. Schäffner [a,*], J. Schieck [e,f], D. Schmiedmayer [e,f], C. Schwertner [e,f], M. Stahlberg [a,*], A. Stendahl [i], F. Wagner [e], S. Yue [h], V. Zema [a,*], Y. Zhu [h], The COSINUS Collaboration, and A. Bento [a,j], L. Canonica [a], A. Garai [a]

[a] *Max-Planck-Institut für Physik, 80805 München, Germany*
[b] *INFN - Sezione di Roma, 00185 Roma, Italy*
[c] *Gran Sasso Science Institute, 67100 L'Aquila, Italy*
[d] *INFN - Laboratori Nazionali del Gran Sasso, 67010 Assergi, Italy*
[e] *Institut für Hochenergiephysik der Österreichischen Akademie der Wissenschaften, 1050 Wien, Austria*
[f] *Atominstitut, Technische Universität Wien, 1020 Wien, Austria*
[g] *Dipartimento di Scienze Fisiche e Chimiche, Università degli Studi dell'Aquila, 67100 L'Aquila, Italy*
[h] *SICCAS - Shanghai Institute of Ceramics, Shanghai, 200050, PR China*
[i] *Helsinki Institute of Physics, Univ. of Helsinki, 00014 Helsinki, Finland*
[j] *LIBPhys-UC, Physics Departments, University of Coimbra, 3004-516 Coimbra, Portugal*

ARTICLE INFO

Keywords:
Cryogenics
Detectors
TES
Phonons
Dark matter
Rare event search

ABSTRACT

Low-temperature calorimeters based on a readout via Transition Edge Sensors (TESs) and operated below 100 mK are well suited for rare event searches with outstanding resolution and low thresholds. We present first experimental results from two detector prototypes using a novel design of the thermometer coupling denoted *remoTES*, which further extends the applicability of the TES technology by including a wider class of potential absorber materials. In particular, this design facilitates the use of materials whose physical and chemical properties, as e.g. hygroscopicity, low hardness and low melting point, prevent the direct fabrication of the TES onto their surface. This is especially relevant in the context of the COSINUS experiment (Cryogenic Observatory for SIgnals seen in Next-Generation Underground Searches), where sodium iodide (NaI) is used as absorber material.

With two *remoTES* detector prototypes operated in an above-ground R&D facility, we achieve baseline energy resolutions of σ=87.8 eV for a 2.33 g silicon absorber and σ=193.5 eV for a 2.27 g α-TeO_2 absorber, respectively. *RemoTES* calorimeters offer – besides the wider choice of absorber materials – a simpler production process combined with a higher reproducibility for large detector arrays.

1. Introduction

Low-temperature detectors operated in the temperature region between tens and hundreds of millikelvin make up an important detector class in particle physics. The detection of particles in cryogenic calorimeters is based on the measurement of the tiny temperature increase caused by an energy deposition in an absorber material, by using very sensitive temperature sensors, e.g. Transition Edge Sensors (TESs), Neutron Transmutation Doped-thermistors (NTDs), Kinetic Inductance Detectors (KIDs), or Metallic Magnetic Calorimeters (MMCs) [1,2].

A TES consists of a superconductive thin film operated in the state between the normal conducting and the superconducting phase. Due to the strong temperature dependence of the film resistance in the transition, even tiny temperature increases ($\mathcal{O}$(μK)) induced by very small energy depositions ($\mathcal{O}$(keV)) in the absorber, lead to measurable changes in resistance of $\mathcal{O}(10^{-1}\Omega)$. For many decades, TESs have been a main pillar in the scope of cryogenic imaging spectrometers for earth

* Corresponding authors.
E-mail addresses: florian.reindl@tuwien.ac.at (F. Reindl), karoline.schaeffner@mpp.mpg.de (K. Schäffner), martin.stahlberg@mpp.mpg.de (M. Stahlberg), vanezema@mpp.mpg.de (V. Zema).

https://doi.org/10.1016/j.nima.2022.167532
Received 1 June 2022; Received in revised form 12 September 2022; Accepted 29 September 2022
Available online 6 October 2022
0168-9002/

and space applications. Their use in the rare event search for direct dark matter detection [3–6] and Coherent Elastic Neutrino-Nucleus Scattering (CEνNS) [7,8] by using massive absorbers $\mathcal{O}$(1–100 g) is a very active field of research at the frontier of knowledge.

TESs based on superconducting tungsten thin-films have been developed within the CRESST dark matter search at the Max–Planck Institute for Physics (MPP) in Munich over the last 30 years [9,10]. The current stage is CRESST-III, which uses 200 nm-thick tungsten films directly fabricated onto the surface of absorbers made of Al_2O_3, $CaWO_4$, $LiAlO_2$ and Si. The extraordinary high sensitivity achieved with TESs is one of the cornerstones of CRESST, which is the leading cryogenic experiment for low-mass dark matter search [3,11].

The deposition of the TES thermometer directly onto the absorber ensures an excellent transmission of the non-thermal phonons to the W-film. This coupling of sensor and absorber is the preferred solution as long as the absorber material can withstand[1] the processes necessary for the fabrication of the temperature sensor, i.e. multiple electron-beam evaporation cycles (requiring temperatures above 700 °C), sputtering, chemical etching and photolithography. However, absorber materials that have a low melting point and/or are hygroscopic cannot undergo these processes. Also, sensor fabrication may negatively impact the radiopurity of the absorber crystal. A work-around solution for delicate materials, such as for the sodium iodide (NaI) crystals used in the COSINUS experiment [6], is the so-called composite design [13]: the TES is fabricated onto a separate substrate which in turn is connected to the absorber via an amorphous interface (glue, oil, or grease). In the following we call the TES substrate used in the composite design "carrier" or "carrier crystal". This approach requires the phonons produced by a particle interacting in the absorber to propagate through the interface, the carrier, and finally couple to the TES. A fraction of the signal reaching the interface is lost in this process due to poor phonon transmission in case of an acoustic mismatch between the different materials of the carrier and the absorber [14]. In COSINUS we considered and tested Al_2O_3, Si, $CaWO_4$ and $CdWO_4$ as carrier materials, which all have a high acoustic mismatch to soft absorber materials like NaI. Furthermore, in the case of a very good scintillator like NaI, a carrier crystal which is not fully transparent to the scintillation light will reabsorb part of the light, causing an additional power input to the TES. In this case, the resulting pulse shape in the TES will be a superposition of the NaI scintillation signal and the primary thermal signal [15]. This effect was observed in earlier COSINUS prototypes and will be subject of a future publication. In [16], the authors propose a TES-based detector concept, denoted *remoTES* in the following, which does not suffer from these disadvantages, features a simpler production process, and additionally promises a better detector reproducibility. In a *remoTES* detector, the TES is fabricated onto a separate, *remo*te substrate, which is placed on the copper holder, according to the scheme in Fig. 2. In the following we refer to the TES substrate used in the *remoTES* design as "wafer". The absorber crystal is then equipped with a Au pad (microfabricated thin film or glued foil) that transmits the phonon signal created from an interaction in the absorber to the TES via a gold bonding wire (wedge-bonded, ball-bonded or glued). To our knowledge, experimental works using the TES coupling design proposed in [16] are absent to present date. However, the experiment RICOCHET is considering this design to read out superconducting absorbers for precision measurements of CEνNS [17] and the AMORE experiment [18] utilizes thin gold films as phonon absorbers connected to a MMC [19]. Marrying ease of fabrication with a wide choice of absorber materials, the *remoTES* may be a breakthrough for TES-instrumented calorimeters based on delicate absorber materials like NaI. In this article, we present the first experimental implementation and the first results which demonstrate the potential of such detectors.

[1] Nonetheless the fabrication process might induce stress in the crystal lattice, which is one of the main potential origins of the excess signal at low energies observed in several experiments [12].

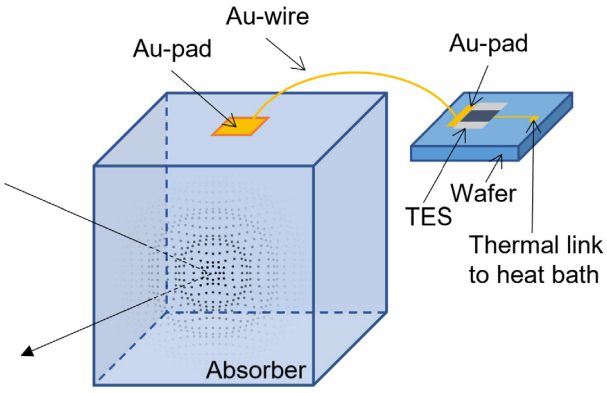

Fig. 1. Schematic view of a *remoTES* detector. The wafer where the TES is fabricated onto (right) is separated from the absorber crystal (left). This crystal is equipped with a gold pad which is linked directly to the TES via a gold bonding wire.

2. Detector design

2.1. Design of the remoTES

The design of a *remoTES* detector is schematically depicted in Fig. 1. It avoids the carrier crystal by coupling the TES directly to the target crystal via a gold pad connected to a gold bonding wire. A significant advantage of this design is that it improves the collection of athermal phonons into the gold pad, which could otherwise be reflected due to the acoustic mismatch between absorber crystal and carrier crystal. Even more importantly, phonons directly couple to the electronic system of the gold pad via electron–phonon coupling [20]. In the literature, this coupling in gold is found to be comparable to or larger than in tungsten [16,21–24]. However, the surface and the thickness of the gold pad have to be carefully optimized: a larger surface enhances the phonon collection efficiency and hence the signal amplitude; at the same time a larger volume increases the total heat capacity, reducing the signal amplitude.

2.2. Design of two remoTES-prototypes

In this manuscript we report the results from two different absorber materials, silicon (Si, 2.33 g) and tellurium dioxide (α-TeO_2, 2.27 g), read out by a *remoTES*. These materials were selected to gain a fundamental understanding of the crucial parameters of this new TES-based readout design. We selected Si as it is a highly-studied standard material for low-temperature application and, thus, useful as a benchmark. We chose α-TeO_2 as a first step on the way to NaI, mainly for its similar solid-state properties, in particular regarding the heat capacity and the gap between the acoustic and optical phonon modes [25,26]. Fig. 2 shows a scheme of α-TeO_2-module. The Si-module is similarly assembled, but the brass screw is not present, as shown in Fig. 3.

Technical details. On the Si absorber ((20x10x5) mm^3) a gold film of circular shape (3 mm diameter) of 200 nm thickness was deposited by Magnetron-sputtering. The connection between the Au pad on the Si absorber and the TES on the wafer was provided via a 17 µm thick and 2–3 mm long Au-bonding wire. While the Au-wire was wedge-bonded onto the Au pad of the TES, it was connected to the Au pad on the Si absorber by using a silver-loaded epoxy (≈25 µg). Avoiding wedge-bonding on the Au pad of the absorber opens up the possibility to also introduce very soft and fragile absorber crystals to this field of research, which would be damaged by solid phase welding processes (e.g. wedge and ball bonding). Alternatively, the Au pad on the TeO_2 absorber ((20x10x2) mm^3) consists of a 400 nm thick Au-foil glued onto its surface by using a two-component epoxy resin.

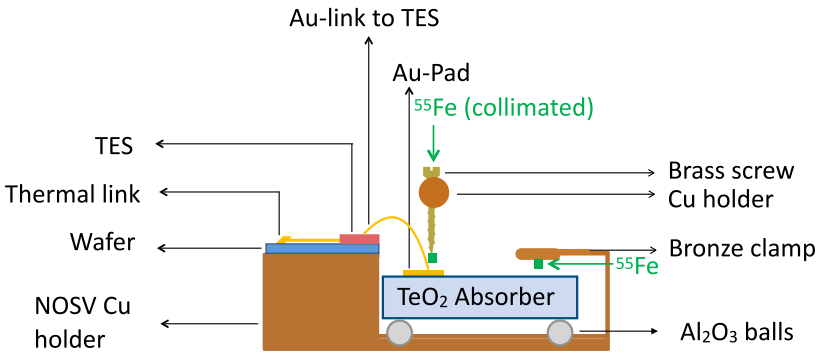

Fig. 2. Scheme of the complete α-TeO_2-module.

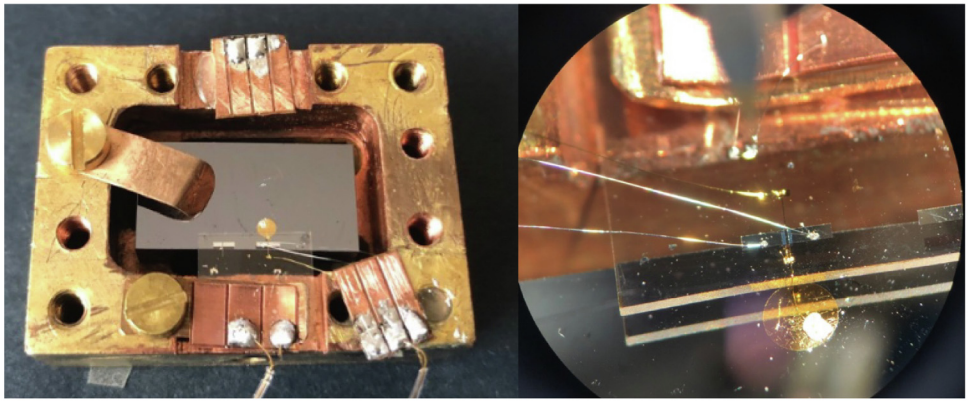

Fig. 3. Left: Image of the Si *remoTES*, surrounded by the Cu housing. Right: Zoomed-in view on the TES and Au pad.

The use of Au foils has two important consequences: a better thermal conductance due to the fact that the Residual Resistance Ratio (RRR) is larger with respect to the sputtered film, and the possibility to avoid any microfabrication process on the crystal surface. The electrical and thermal contact between Au pad on the TeO_2 and the TES was realized with a wedge-bond on both sides, respectively. Table 1 summarizes the condensed information on both prototype detectors. It is worth to mention that the two configurations are not meant to be used for performance comparison, but rather elucidate the flexibility of the *remoTES* concept, and the possibility to adapt it to various absorber materials.

The TES on the thin Al_2O_3 wafer ((10x10x0.4) mm^3) was identical for both measurements. It consists of a 100 nm-thick tungsten film of an area of (220x300) μm^2 and two aluminum pads for biasing of the sensor. The area of the W-film not overlapping with the pads is (70x300) μm^2. The weak thermal link to the heat bath consists of a 1 mm long Au-stripe (20 µm in width, 80 nm in thickness). An additional gold stripe ((200x130) μm^2, 0.1 µm thick) was evaporated on the wafer at about 2.5 mm of distance from the sensor. It is used to inject heat pulses in order to monitor the TES operating point.

3. Experimental results and discussion

The measurements reported here were carried out in a dilution refrigerator of the CRESST group at the Max–Planck Institute for Physics in Munich. This is an above-ground, liquid ^{4}He-precooled dilution refrigerator for R&D measurements and TES testing. It is equipped with four SQUID channels (APS company) and a VME-based data acquisition using a hardware-triggered readout. The total exposure was 1.06 g·d for the Si detector and 2.28 g·d for TeO_2. For the purpose of energy calibration both prototype detectors were irradiated by an uncollimated ^{55}Fe-source shining onto the side of the absorber opposite to the face with the Au pad. Furthermore, the TeO_2 detector was equipped with an additional collimated ^{55}Fe-source irradiating solely the Au pad glued onto the absorber.

Table 1
Summary of the two measurements using the *remoTES* design. RRR = Residual Resistance Ratio.

Absorber material	Si	TeO_2
Absorber volume (mm^3)	20 × 10 × 5	20 × 10 × 2
Au pad properties	200 nm sputtered RRR = 3.79	400 nm foil glued RRR = 15
Au-wire properties	17 µm glued on pad	17 µm 2 wedge bonds
TES	W-TES on Al_2O_3	W-TES on Al_2O_3
Baseline resolution (eV)	87.8 ± 5.6	193.5 ± 3.1

3.1. Data analysis

We observe different event classes in both detectors. Standard events (SEVs = averaged pulses scaled to an amplitude of 1 V) for these classes are shown in Fig. 4; they were created from a small, selected sample of pulses with the same shape for each class. For both detectors, there is a dominant class of events, depicted in green, which is characterized by a (10%–90%) rise time of ≈1 ms, with a (90%–10%) decay time of ≈44 ms for the Si prototype, and ≈122 ms for the TeO_2 prototype. The high rate of these events (cf. Table 2) is consistent with hits in the absorber, considering that the ^{55}Fe source shining on the "bottom" of the absorber cannot be seen by the wafer carrying the TES. Hits in the latter (orange in Fig. 4) feature much faster signals: the rise times are only ≈0.16 ms (Si measurement) and

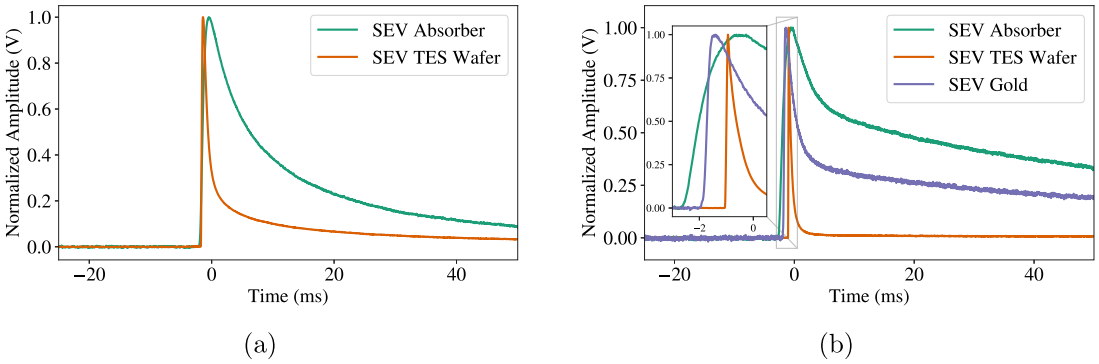

Fig. 4. Standard events (SEVs) for the two prototype detectors. (a) Events in the Si absorber (green) and the TES wafer (orange). (b) Events in the TeO_2 absorber (green), the TES wafer (orange) and the gold pad on the TeO_2 (violet). The pulse onsets for each event class are slightly shifted for visualization purposes.

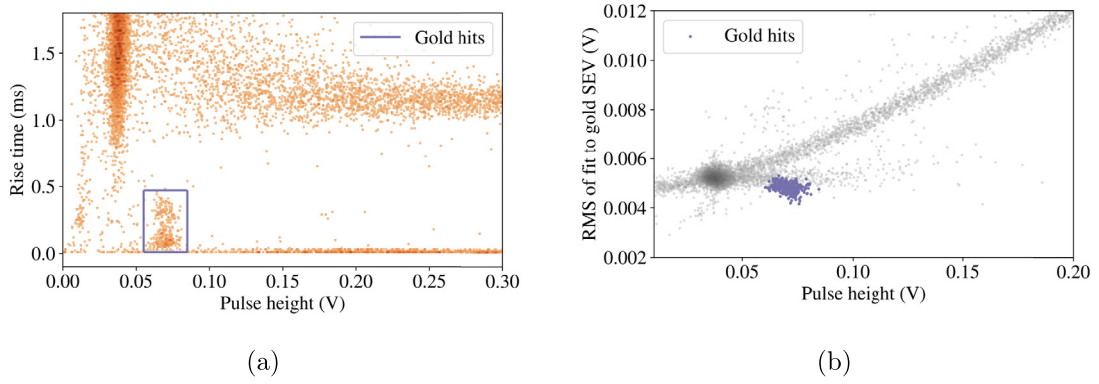

Fig. 5. TeO_2-*remoTES* dataset: (a) Rise time versus moving average pulse height distribution. The violet box encloses the events in the gold foil produced by the collimated ^{55}Fe-source. (b) Fit RMS for the gold SEV as a function of the pulse height distribution. The events from the violet box in panel (a) are tagged and depicted in violet.

≈0.07 ms (TeO_2 measurement), while the decay times are ≈11.2 ms and ≈1.2 ms, respectively.

The TeO_2 prototype exhibits an additional event class. We identify these comparatively rare events (cf. Table 2) as hits from the collimated ^{55}Fe-source irradiating the Au pad on the absorber. The rise time of the pulse is driven by the time needed to transport energy to the TES which depends on the energy carriers. The transport is fast for electrons and non-thermal phonons, which are the dominant energy carriers for the events created by interactions in the Au pad or the wafer. In the TeO_2 absorber, a larger part of the initial phonon population undergoes thermalization, consequently leading to slower pulses. The Au pad events are visible in Fig. 5(a) as a cluster of events in the violet box. Their decay time is faster than the one of absorber events, but slower than the one of wafer events. The explanation for the difference between gold and wafer events can be two-fold: firstly, energy deposited in the Au pad is partially transmitted back and forth to and from the absorber, leading to a larger decay time; secondly, the heat capacity of Au affects the decay time, leading to even slower pulses. The Au pad is small in comparison to the absorber, and connected directly to the TES. Therefore, pad events in Fig. 5(a) are distributed around a larger pulse height (∼ 0.07 V) with respect to the pulse height of the ^{55}Fe-events in the absorber (∼ 0.04 V).

Few basic quality cuts are applied to the complete dataset: events coinciding with a decaying baseline from a previous pulse are removed by placing a cut on the pre-trigger baseline slope. Additionally, events with a reconstructed pulse onset more than 1 ms away from the trigger position are discarded. To separate different event classes reliably, the root mean square (RMS) from a truncated standard event fit is used. This method is described in e.g. [11]: a SEV is fitted to a subset of samples for each pulse, where only samples below a given truncation limit (relative to the baseline) are considered. We fit each pulse with all three SEVs, and the dataset for each event contains only those events where the respective fit yields the lowest RMS. As an example, the discrimination between absorber and wafer events is shown in Fig. 6. Fig. 5(a) illustrates the discrimination between absorber events and ^{55}Fe Au pad events: The latter are marked in violet, and have been identified as a cluster in Fig. 5(a) using their fast rise time. Table 2 shows the number of surviving events for each prototype and event class; as stated before, absorber events are the dominant event class in

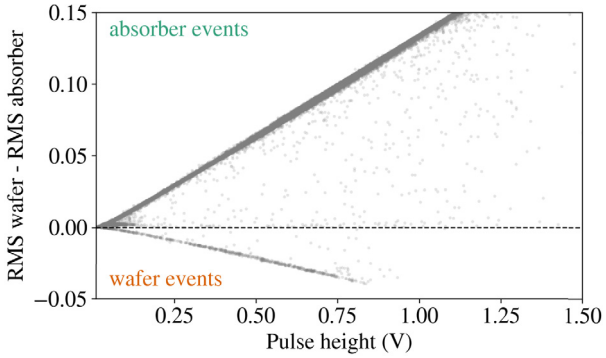

Fig. 6. Difference between RMS values from the wafer SEV fit and the absorber SEV fit as a function of moving-average pulse height for the TeO_2 prototype; different event bands corresponding to the different classes are visible. The event population between the absorber and the wafer band corresponds to the Au hits; its pulse shape is a mixture of the former two classes, and their shapes match it equally well.

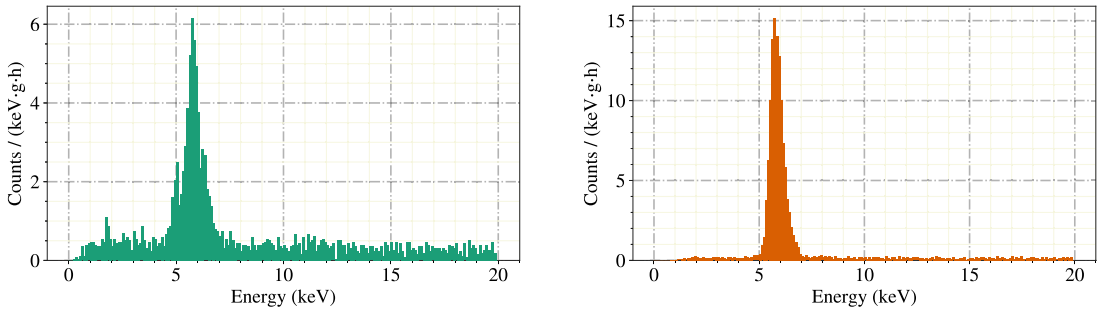

Fig. 7. The energy spectra of the two prototype detectors: (a) Si absorber and (b) TeO_2 absorber. The intensity of the ^{55}Fe-source producing X-rays of 5.89 keV (K_α) and 6.49 keV (K_β) was significantly stronger for (b). The energies of the additional peaks in the Si detector (≈1.8 keV and ≈5 keV) are consistent with X-ray emission from the K-shell of Si (1.84 keV), and an escape line due to the Cu holder (Cu L_α at 0.93 keV).

Table 2
Number of surviving events after quality cuts for each measurement and event class (see text for details).

Absorber material	"Absorber" events	"Wafer" events	"Gold" events
Si	6072	398	–
TeO_2	28555	711	314

both measurements, and Au-hits are less frequent than wafer hits for the TeO_2 detector.

In addition to the events produced by particles interacting in the active detector parts, we periodically inject electrical pulses with known amplitudes into the heater of each detector. These heater pulses allow monitoring the detector response over time, and accounting for nonlinearity and the effect of saturation in the TES, which influence the pulse shape at high energies (see e.g. [11]). A truncated fit with a dedicated heater SEV is performed for all heater pulses, and the resulting amplitude is used in combination with the input pulser setting to compensate non-linearities and time-variations of the reconstructed (fitted) amplitude for particle-induced events [27].

3.2. Energy calibration and resolution

The K_α peak from the ^{55}Fe source (5.89 keV) prominent in the spectrum of the Si and TeO_2 detector is used to calibrate the detector response, which is given by the truncated fit result for absorber events corrected by the heater response information. We chose the truncated fit over the usual method of optimal filtering [28] here, since the noise conditions in both measurements changed over time, and the filter relies on a stable noise power spectrum. The resulting spectra for absorber events are given in Fig. 7. For the TeO_2 detector, K_α and K_β lines are not resolved, and the left flank of the single peak structure was used for calibration.

The baseline resolution is determined for each detector in the following way: in each measurement, records without a trigger event are taken in regular intervals. These "empty baselines" are then cleaned, removing random coincidences with pulses and artifacts. Subsequently, we superimpose the SEV for a given detector with all remaining empty baselines. These artificial events (122 for the Si detector and 1932 for TeO_2) are passed through the analysis chain and reconstruction algorithm, and the detector resolution is extracted from the reconstructed amplitudes. The resolutions (all in σ) are (18.4 ± 1.2) mV for the Si and (1.22 ± 0.02) mV for the TeO_2 absorber, corresponding to (87.8 ± 5.6) eV and (193.5 ± 3.1) eV, respectively (cf. Table 1). Typically, the achievable threshold of a TES is about five times the baseline resolution.

4. Conclusion

The *remoTES* is an alternative design of the TES coupling to the absorber in a cryogenic calorimeter. It can be used in combination with delicate absorber materials such as NaI, which cannot withstand the process of direct TES fabrication. In this work we presented the successful operation of two *remoTES* detector prototypes using a Si and a TeO_2 absorber in above-ground measurements, achieving 1σ baseline resolutions of 87.8 eV and 193.5 eV, respectively. We observed two event classes with distinctively different pulse shapes in each detector, which result from particle interactions in the absorber and in the wafer of the TES. Additionally, a third event class was made visible in the TeO_2 measurement using an additional ^{55}Fe source irradiating the Au pad glued onto the absorber. This event class featured a very low rate and long pulse decay time, consistent with hits in the pad. We already performed first measurements with NaI absorbers which will be discussed in future publications. Compared to "composite-type" detectors, the *remoTES* improves phonon propagation from the absorber to the sensor, if absorber and carrier are made of different materials [29]. This design additionally prevents the undesirable collection of scintillation light in the carrier. Furthermore, the separately fabricated wafer-TES can be reused with a different target — this implies an improved reproducibility for *remoTES* detectors with respect to their carrier design counterparts, and greatly facilitates comparisons between different absorber materials.

In summary, our results show that the TES technology can be successfully used with almost any absorber. Materials that required the use of a carrier crystal in the past can now be operated without such a crystal by simply adding a gold interface. Even for "standard" absorbers, the use of a *remoTES* avoids exposing the material to fabrication processes, thus preserving the initial radiopurity and lattice condition of the absorber crystal. Indeed, the *remoTES* concept gives the possibility to use materials such as NaI for standard WIMP searches, and its use may be extended to other fields like neutrinoless double β decay and CEνNS.

Declaration of competing interest

The authors declare that they have no known competing financial interests or personal relationships that could have appeared to influence the work reported in this paper.

Data availability

Data will be made available on request.

Acknowledgments

This work was carried out in the frame of the COSINUS collaboration. We would like to acknowledge Matt Pyle, Enectali Figueroa-Feliciano and Bernard Sadoulet who had the idea of developing TES-based detectors of such kind, as published already in 2015 on arXiv:1503.01200 [16]. The data analysis was mainly carried out with collaboration-internal software tools, and partially with the open source Python package CAIT [30]. We want to thank the MPP mechanical workshop team for in-time support in all needs regarding the cryogenic facility and detector holder fabrication. We are grateful to the colleagues from the CRESST MPP group for sharing the infrastructure for detector production, the wet dilution refrigerator facility for the measurements and their cryogenic expertise and experience. In particular we thank Ahmed Abdelhameed for many insightful discussions on thin-film technology.

References

[1] C. Enss, D. Mccammon, Physical principles of low temperature detectors: ultimate performance limits and current detector capabilities, J. Low Temp. Phys. 151 (1) (2008) 5–24, http://dx.doi.org/10.1007/s10909-007-9611-7.

[2] Y. Kim, S. Lee, B. Yang, Superconducting detectors for rare event searches in experimental astroparticle physics, Supercond. Sci. Technol. 35 (6) (2022) 063001.

[3] A.H. Abdelhameed, et al., CRESST Collaboration Collaboration, First results from the CRESST-III low-mass dark matter program, Phys. Rev. D 100 (10) (2019) 102002, http://dx.doi.org/10.1103/PhysRevD.100.102002.

[4] I. Alkhatib, et al., SuperCDMS Collaboration Collaboration, Light dark matter search with a high-resolution athermal phonon detector operated above ground, Phys. Rev. Lett. 127 (6) (2021) 061801, http://dx.doi.org/10.1103/PhysRevLett.127.061801.

[5] R. Agnese, et al., SuperCDMS Collaboration Collaboration, Search for low-mass dark matter with CDMSlite using a profile likelihood fit, Phys. Rev. D 99 (6) (2019) 062001, http://dx.doi.org/10.1103/PhysRevD.99.062001.

[6] G. Angloher, et al., COSINUS Collaboration Collaboration, The COSINUS project: perspectives of a NaI scintillating calorimeter for dark matter search, Eur. Phys. J. C 76 (8) (2016) 441, http://dx.doi.org/10.1140/epjc/s10052-016-4278-3, (ISSN: 1434-6044, 1434-6052).

[7] G. Angloher, et al., Exploring CEνNS with NUCLEUS at the Chooz nuclear power plant, Eur. Phys. J. C (ISSN: 1434-6052) 79 (12) (2019) 1018, http://dx.doi.org/10.1140/epjc/s10052-019-7454-4.

[8] J. Billard, et al., Coherent neutrino scattering with low temperature bolometers at Chooz reactor complex, J. Phys. G: Nucl. Part. Phys. (ISSN: 0954-3899) 44 (10) (2017) 105101, http://dx.doi.org/10.1088/1361-6471/aa83d0.

[9] W. Seidel, et al., Phase transition thermometers with high temperature resolution for calorimetric particle detectors employing dielectric absorbers, Phys. Lett. B 236 (4) (1990) 483–487, http://dx.doi.org/10.1016/0370-2693(90)90388-M.

[10] R. Strauss, et al., The CRESST-III low-mass WIMP detector, J. Phys. Conf. Ser. 718 (4) (2016) 042048.

[11] G. Angloher, et al., Results on MeV-scale dark matter from a gram-scale cryogenic calorimeter operated above ground, Eur. Phys. J. C 77 (9) (2017) 637, http://dx.doi.org/10.1140/epjc/s10052-017-5223-9, (ISSN: 1434-6044, 1434-6052).

[12] P. Adari, et al., in: A. Fuss, M. Kaznacheeva, F. Reindl, F. Wagner (Eds.), EXCESS Workshop: Descriptions of Rising Low-Energy Spectra, 2022, http://dx.doi.org/10.48550/arXiv.2202.05097, arXiv:2202.05097.

[13] G. Angloher, et al., Composite $CaWO_4$ detectors for the CRESST-II experiment, in: AIP Conference Proceedings, Vol. 1185, AIP Publishing, 2009, pp. 651–654, http://dx.doi.org/10.1063/1.3292426.

[14] K.E. Gray, Nonequilibrium superconductivity, phonons, and Kapitza boundaries, Springer Sci. Bus. Media 65 (Chapter 1) (2012) http://dx.doi.org/10.1007/978-1-4684-3935-9.

[15] V. Zema, Unveiling the Nature of Dark Matter with Direct Detection Experiments (Ph.D. thesis), Gran Sasso Science Institute, Chalmers U. Tech, 2020, URL https://inspirehep.net/literature/1813204.

[16] M. Pyle, et al., Optimized Designs for Very Low Temperature Massive Calorimeters, 2015, http://dx.doi.org/10.48550/arXiv.1503.01200, arXiv:1503.01200.

[17] R. Chen, Ricochet Collaboration, Transition edge sensor chip design of modular CEνNS detector for the ricochet experiment, 2021, arXiv. arXiv:2111.05757. http://dx.doi.org/10.48550/arXiv.2111.05757.

[18] V. Alenkov, et al., First results from the AMoRE-pilot neutrinoless double beta decay experiment, Eur. Phys. J. C 79 (9) (2019) 791, http://dx.doi.org/10.1140/epjc/s10052-019-7279-1, arXiv:1903.09483.

[19] Y.H. Kim, et al., Measurements and modeling of the thermal properties of a calorimeter having a sapphire absorber, Nucl. Instrum. Methods Phys. Res. A (ISSN: 0168-9002) 520 (1) (2004) 208–211, http://dx.doi.org/10.1016/j.nima.2003.11.230, Proceedings of the 10th International Workshop on Low Temperature Detectors.

[20] W. Little, The transport of heat between dissimilar solids at low temperatures, Can. J. Phys. 37 (3) (1959) 334–349, http://dx.doi.org/10.1139/p59-037.

[21] F. Pröbst, et al., Model for cryogenic particle detectors with superconducting phase transition thermometers, J. Low Temp. Phys. 100 (1–2) (1995) 69–104, http://dx.doi.org/10.1007/BF00753837, (ISSN: 0022-2291, 1573-7357).

[22] M. Sisti, et al., Massive cryogenic particle detectors with low energy threshold, Nucl. Instrum. Methods Phys. Res. A 466 (3) (2001) 499–508, http://dx.doi.org/10.1016/S0168-9002(01)00801-4.

[23] J. Karvonen, et al., Electron–phonon interaction in thin copper and gold films, Phys. Status Solidi (C) 1 (11) (2004) 2799–2802, http://dx.doi.org/10.1002/pssc.200405326.

[24] S. Hart, et al., Phase separation in tungsten transition edge sensors, in: AIP Conference Proceedings, Vol. 1185, American Institute of Physics, 2009, pp. 215–218, http://dx.doi.org/10.1063/1.3292318.

[25] A. Jain, et al., The materials project: A materials genome approach to accelerating materials innovation, APL Mater. 1 (011002) (2013) http://dx.doi.org/10.1063/1.4812323.

[26] Y. Hinuma, et al., Band structure diagram paths based on crystallography, Comput. Mater. Sci. 128 (2017) 140–184, http://dx.doi.org/10.1016/j.commatsci.2016.10.015.

[27] G. Angloher, et al., Limits on WIMP dark matter using sapphire cryogenic detectors, Astropart. Phys. (ISSN: 0927-6505) 18 (1) (2002) 43–55, http://dx.doi.org/10.1016/S0927-6505(02)00111-1.

[28] E. Gatti, P.F. Manfredi, Processing the signals from solid-state detectors in elementary-particle physics, Riv. Nuovo Cimento (ISSN: 1826-9850) 9 (1) (1986) 1–146, http://dx.doi.org/10.1007/BF02822156.

[29] K. Schäffner, et al., Particle discrimination in TeO_2 bolometers using light detectors read out by transition edge sensors, Astropart. Phys. 69 (2015) 30–36, http://dx.doi.org/10.1016/j.astropartphys.2015.03.008.

[30] F. Wagner, et al., Fewagner/Cait: V1.0.0, Zenodo, 2021, http://dx.doi.org/10.5281/zenodo.5091416.